Available online at www.sciencedirect.com
ScienceDirect
Trans. Nonferrous Met. Soc. China 24(2014) 423−430
Transactions of Nonferrous Metals Society of China
www.tnmsc.cn

Influence of Al−Mn master alloys on microstructures and electrochemical properties of Mg−Al−Pb−Mn alloys

Bin CHEN, Ri-chu WANG, Chao-qun PENG, Yan FENG, Nai-guang WANG

School of Materials Science and Engineering, Central South University, Changsha 410083, China

Received 24 January 2013; accepted 22 May 2013

Abstract: Mg−Al−Pb alloy is one of the newly developed materials for the seawater activated batteries. As-cast Mg−6Al−5Pb and Mg−6Al−5Pb−0.5Mn alloys with different additions of Al−15%Mn (mass fraction), Al−30%Mn and Al−50%Mn master alloys were prepared by melting and casting. Their microstructures were observed by optical microscopy and scanning electron microscopy. The electrochemical properties, hydrogen evolution and mass loss of Mg−6Al−5Pb−0.5Mn alloys were studied. The results show that Mg−6Al−5Pb−0.5Mn alloy added with Al−50%Mn master alloy provides more negative corrosion average potential (−1.66 V), smaller corrosion current density (7 μm/cm^2) and lower free corrosion rate (0.51 mg·cm^{-2}·h^{-1}) than other alloys. This is probably attributed to the presence of $Al_{11}Mn_4$ phase, which facilitates the self-peeling of corrosion products and enlarges the electrochemical reaction area as well as enhances the electrochemical activity.

Key words: Al−Mn; master alloy; Mg−Al−Pb−Mn; hydrogen evolution; corrosion; seawater activated batteries

1 Introduction

Magnesium alloys are typically utilized in military applications [1,2] as the anode material of seawater battery of electric torpedo, as the power sources for buoys, air-sea rescue equipment, weather balloons, marine markers, communications and underwater propulsion [3,4]. Seawater batteries rely on the corrosion of a reactive metal anode, which increases the cell voltages and minimizes the self-discharge [5]. However, poor corrosion resistance is the bottlenecks of wide use of magnesium alloys [6,7].

Alloying magnesium with aluminum in general improves the corrosion resistance. It is reported that the corrosion rate decreases rapidly with increasing aluminum content up to 4%. Further increasing aluminum content up to 9% gives only a modest further improvement [6,8,9]. Pb element is an effective element and able to precipitate on the surface as well as facilitate the precipitation of $Mg(OH)_2$ film and activate the magnesium matrix [10,11]. Manganese has low solubility and diffuses slowly in the matrix [12]. It plays a critical role in the development as an iron remover. Thereby, it is necessary to investigate the effect of manganese on magnesium alloys. Mg−Al−Mn ternary diagram shows that Al_8Mn_5 and $Al_{11}Mn_4$ phases can coexist with Mg−Al melt in a wide temperature range. This means manganese aluminides are promising candidates for reinforcement phases in the magnesium alloys and play an important role on the electrochemical discharge behavior. A few reports have investigated the effect of manganese aluminides on grain size. YE and LIU [13] reported that manganese additive using pure manganese with an irregular and less than 45 μm in size has potential influence on the grain size. JÖNSSON et al [14] prepared magnesium containing β and Al_8Mn_5 particles and found that Al_8Mn_5 particle works as stronger cathode when coupled to the magnesium than β phase. PENG et al [15] studied that manganese was added in the form of Al−60%Mn alloy for magnesium and can be a grain refiner.

Some researchers pay attention to manganese additive on the grain refiner of magnesium alloys. However, there are few reports in relation to manganese on the electrochemical behavior of magnesium alloys. Despite the extensive research on the corrosion behavior, there is lack of detailed or systematic study on the corrosion mechanism. In this work, the effect of manganese additive on the microstructures and the

Foundation item: Project (JPPT-115-168) supported by the National Key Science and Technological Project of China; Project (51101171) supported by the National Natural Science Foundation of China
Corresponding author: Ri-chu WANG; Tel: +86-731-88836638; E-mail: wrc@mail.csu.edu.cn
DOI: 10.1016/S1003-6326(14)63078-8

electrochemical corrosion performances of Mg−6Al−5Pb−0.5Mn alloys with the addition of Al−15%Mn, Al−30%Mn and Al−50%Mn master alloys were investigated.

2 Experimental

Al−15%Mn, Al−30%Mn and Al−50%Mn master alloys were fabricated by inductive melting and analyzed by XRD. Subsequently, AP65 and Mg−6Al−5Pb−0.5Mn alloys were smelted with high purity magnesium (>99.99%), aluminium (>99.9999%), lead (>99.999%), by electrical resistance furnace at 760 °C under the protection of coating agent and refining flux. The melts were held for 10 min and poured into mild steel moulds under the protection of sulfur powder and cooled at air to room temperature. AP65 alloys with the addition of Al−15%Mn, Al−30%Mn and Al−50%Mn master alloys were denoted as AP65(15Mn), AP65(30Mn) and AP65(50Mn) alloys, respectively. The compositions of the AP65 alloys were test by inductively coupled plasma atomic emission spectrophotometry (ICP-AES), as listed in Table 1.

Table 1 Composition of AP65 alloys (mass fraction,%)

Alloy	Composition/%					
	Al	Pb	Mn	Fe	Cu	Mg
AP65	6.15	5.04	0.002	0.003	0.005	Bal.
AP65(15Mn)	6.13	5.08	0.535	0.008	0.008	Bal.
AP65(30Mn)	6.09	5.11	0.522	0.006	0.007	Bal.
AP65(50Mn)	6.11	5.19	0.518	0.005	0.003	Bal.

The microstructures of the ingots polished using 0.5 μm diamond paste and etched with solution (1 g oxalic acid +1 mL concentrated nitric acid +1 mL acetic acid +150 mL distilled water) were observed with an XJP-6A optical microscope (OM), a JXA-8230 electron probe micro-analyzer (EPMA) and a Quanta-200 scanning electron microscope (SEM) with an energy dispersive spectroscopy (EDS).

All of the samples used for electrochemical tests were moulded into epoxy resin with one side unsealed with a size of 10 mm×10 mm, ground to 1200 grit SiC paper. The potentiodynamic polarization, galvanostatic, electrochemical impedance spectroscopy (EIS) of AP65 alloys were studied in 3.5% NaCl neutral solution by IM6ex potentiostat. A classical three-electrode cell was composed of platinum gauze as the counter electrode, saturated calomel electrode (SCE, 0.242 V vs SHE) as the reference electrode, and the samples as the working electrode. Potentiodynamic polarization measurements began from cathodic side (approximately away from Open Circuit Potential 250 mV) at a constant scan rate of 2 mV/s. The corroded morphologies of specimens after galvanostatic tests for about 5 s and 600 s were observed with SEM. The scan frequency of electrochemical impedance spectroscopy (EIS) ranged from 100 kHz to 50 mHz and the perturbation amplitude was 5 mV. The initial 600 s was set to obtain a stable testing system by immersing the specimens into seawater at open circuit potential. The experimental data were fitted with Z-view software.

The corrosion behaviors for the AP65 alloys were investigated by immersion test. Before test, the specimens were ground successively to 1200 grit SiC paper and weighed. After the corrosion products were cleaned, the specimens were weighed again to determine the mass loss rates caused by corrosion during immersion tests. The hydrogen evolution volumes were measured using gas apparatus [7].

3 Results and discussion

3.1 Microstructures

The XRD patterns of Al−*x*Mn (*x*=15%, 30% and 50%) master alloys (see Fig. 1) indicate that Al, Al_6Mn, and Al_4Mn phases are present for Al−15%Mn master alloy; Al−30%Mn master alloy has Al and Al_8Mn_5 phases; there are Al, $Al_{11}Mn_4$ and Al_8Mn_5 phases for Al−50%Mn alloy. $Al_{11}Mn_4$ phase is probably transformed from *ε*-AlMn phase when the temperature drops during the non-equilibrium solidification [16].

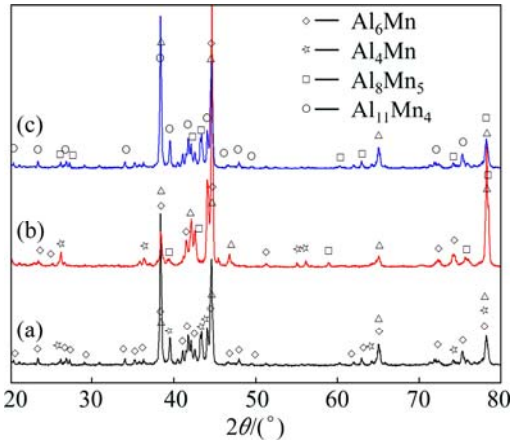

Fig. 1 XRD patterns of Al−15%Mn (a), Al−30%Mn (b) and Al−50%Mn (c) master alloys

Figure 2 shows the optical microstructure of as-cast AP65 alloys. AP65 alloys typically have a primary *α*-Mg matrix and divorced eutectic phase distributed along the grain boundaries. Al−Mn phases are uniform and homogeneously dispersed in the Mg matrix. The amount of second phases increases firstly with the increase of Mn amount of the Al−Mn master alloy and then decreases. When the Mn content is up to 30%, the amount of second phases is close to the maximum.

AP65(50Mn) alloy has smaller grains and more uniform microstructure than AP65 alloy, and AP65 alloy has some micro-pores (see Figs. 3(a) and (d)).

Table 2 lists the mole compositions of points *A*, *B*, *C* and *D* in Fig. 4, which were obtained by quantitative EPMA. EPMA results show that the average molar ratios of Al/Mn for AP65(15Mn), AP65(30Mn) and AP65(50Mn) alloys are 3.72, 1.76 and 2.4, respectively, which correspond to the ranges of stoichiometric ratios of Al_4Mn, Al_8Mn_5 and $Al_{11}Mn_4$ phases, respectively. Al_4Mn phase has a club-shaped morphology (Fig. 4(a)). Al_8Mn_5 phase principally has a polygonal morphology and displays a rod-like morphology (Figs. 4(b) and (c)), which is consistent with Refs. [17,18]. $Al_{11}Mn_4$ phase (Fig. 4(d)) has a quadrilateral shape.

Table 2 Contents of points *A*, *B*, *C* and D (mole fraction, %)

Point	*x*(Mg)/%	*x*(Al)/%	*x*(Mn)/%
A	15.65	65.74	18.62
B	2.70	60.47	36.85
C	7.20	58.67	34.08
D	16.00	59.31	24.68

3.2 Electrochemical properties

Figure 5 illustrates the typical polarization and galvanostatic curves of AP65 alloys. The polarization curves are not symmetrical between their anodic and cathodic branches. These potentiodynamic curves do not exhibit Tafel behavior in the anodic branch. In contrast, the cathodic branch exhibits linear Tafel behavior. Much

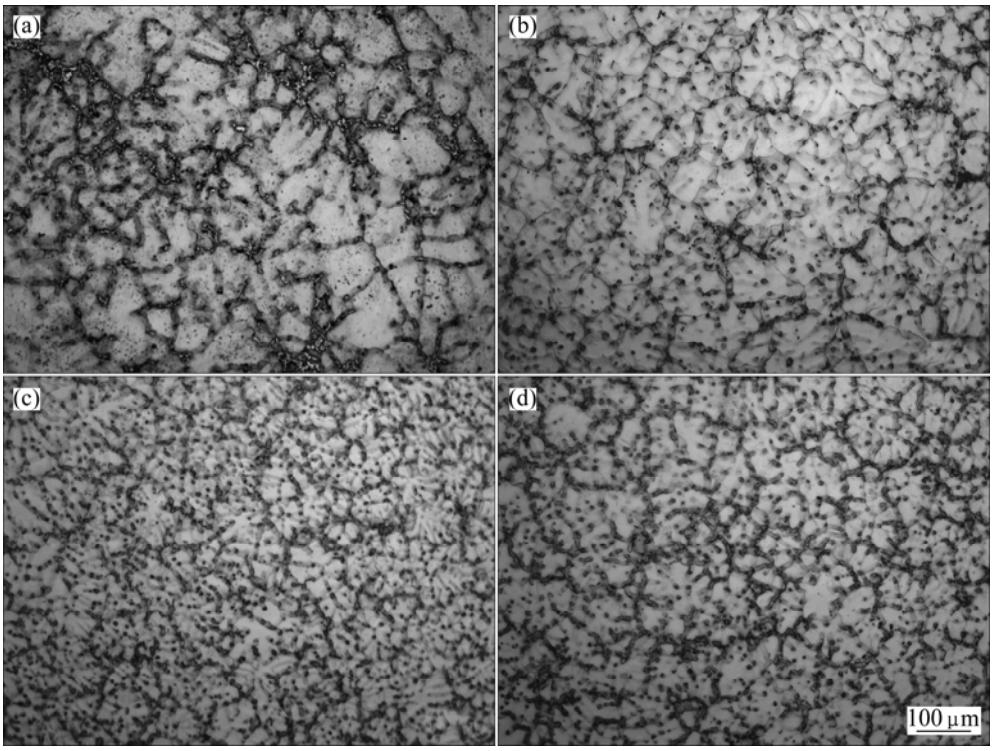

Fig. 2 Optical microstructures of AP65 (a), AP65(15Mn) (b), AP65(30Mn) (c) and AP65(50Mn) (d) alloys

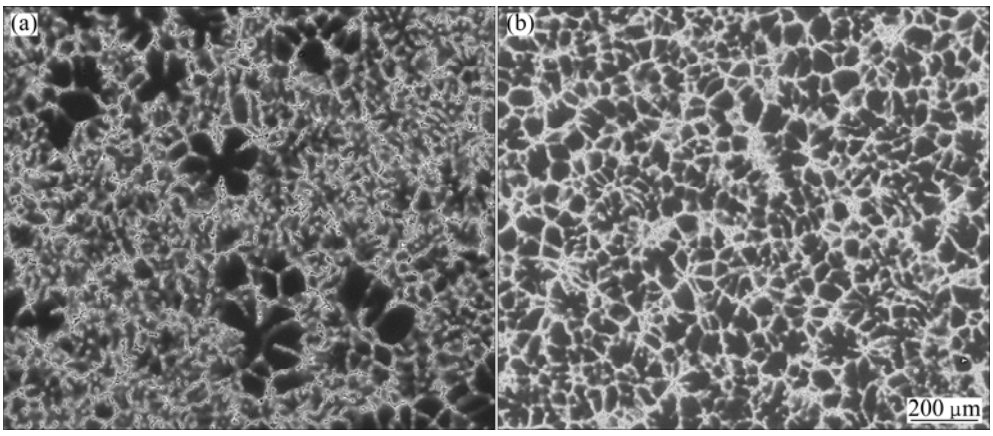

Fig. 3 Back-scattered electron images of AP65 (a) and AP65(50Mn) (b) alloys

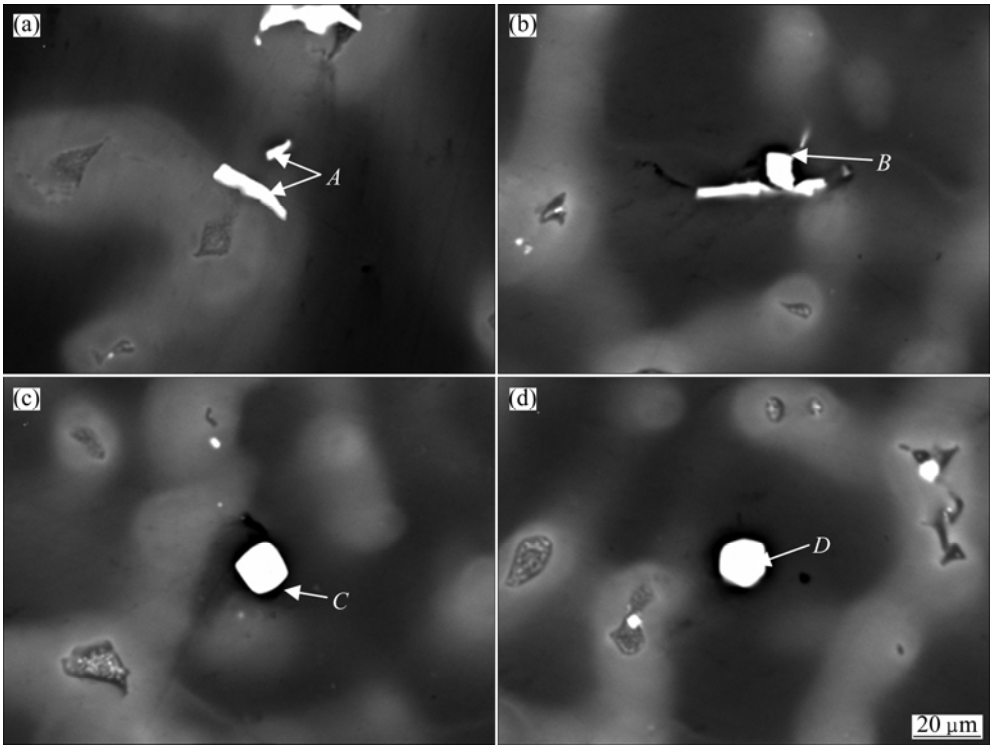

Fig. 4 SEM images of as-cast AP65 (a), AP65(15Mn) (b), AP65(30Mn) (c) and AP65(50Mn) (d) alloys

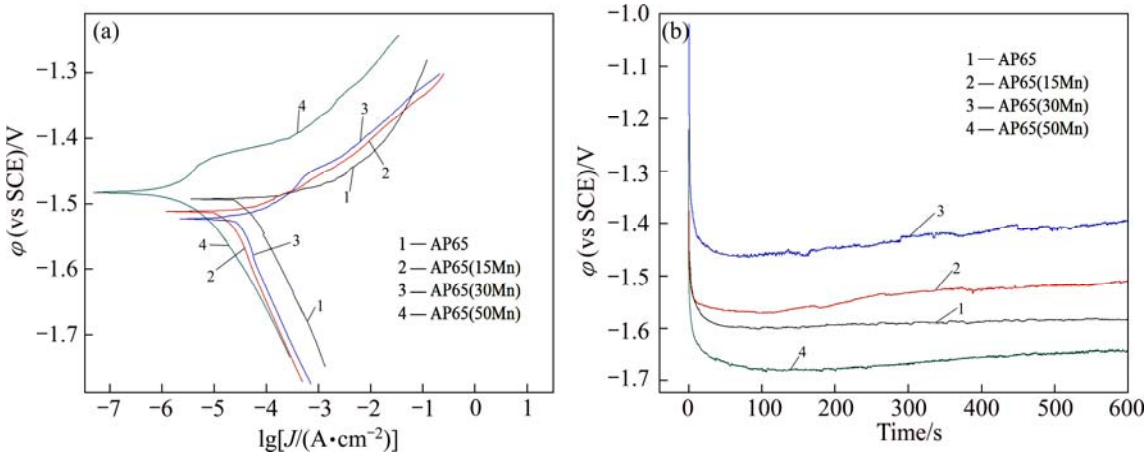

Fig. 5 Potentiodynamic polarization (a) and galvanostatic (b) curves of as-cast AP65 alloys

sharper changes in lg|J| versus imposed potential curves were observed in the anodic polarization branches than in cathodic polarization branches. All these polarizations have similar shapes. This reveals that their corrosion is anodically controlled [19,20]. The polarization parameters measured from the polarization curves are given in Table 3. The corrosion current density (J_{corr}) is fitted by Tafel linear extrapolation method by Z-view software. The results show slight variations in the corrosion potential and the corrosion current density of AP65 alloys. The most positive value of φ_{corr} corresponds to the minimum value of the corrosion rate [21]. The corrosion potential of AP65(50Mn) alloy is the most positive (−1.483 V). The corrosion potential shifts positively by 40 mV from AP65(50Mn) alloy to AP65 alloy. Meanwhile, the corrosion current density decreases from 24.6 to 7 μA/cm^2. So, AP65(50Mn) alloy is the least susceptible to corrosion.

Table 3 Corrosion potential, corrosion current density and average potential of AP65 alloys

Alloy	φ_{corr} (vs SCE)/V	J_{corr}/(μA·cm^{-2})	φ_{mean}/V
AP65	−1.493	10.02	−1.59
AP65(15Mn)	−1.512	17.00	−1.56
AP65(30Mn)	−1.523	24.60	−1.43
AP65(50Mn)	−1.483	7.00	−1.66

The magnesium anode with terrific electrochemical performance exhibits strong activity and provides a far more negative mean potential with a short transition time

for the potential to reach the steady state. During the galvanostatic test, both cathode and anode liberate substantial hydrogen. This demonstrates that the dynamic balance is established among the formation, deposition and desquamating of the corrosion products. Thereby, their activation mechanism is dissolution-reprecipitation [16]. AP65(50Mn) alloy has the shortest transition time and discharges more steadily among these alloys.

The standard potential of magnesium is −2.73 V. This deviation in practical and ideal potential is due to the formation of a magnesium hydroxide film on the metal surface. The mean potentials of AP65 alloys are listed in Table 2. It shows that AP65(50Mn) alloy has the most negative steady-state potential (−1.66 V (vs SCE)) than the other alloys. The more mean potential is beneficial for utilization as anode in the seawater activated battery. This indicates that AP65(50Mn) alloy has outstanding electrochemical activity and offers a higher specific energy. Accordingly, that using Al−50%Mn as additive is advantageous.

The Nyquist plots of AP65 alloys are shown in Fig. 6(a). The alloys exhibit two capacitive loops. One (the bigger one) is for high and intermediate frequencies and the other is for low frequencies. All of AP65 alloys have similar EIS shape with a little difference in the R_t. The charge transfer resistance reduces in the following order: AP65(30Mn) alloy > AP65(15Mn) alloy > AP65 alloy > AP65(50Mn) alloy. Generally speaking, the charge transfer resistance is inversely proportional to the electrochemical activity of magnesium alloys [22]. The electrochemical activity reduces in the following order: AP65(50Mn) alloy >AP65 alloy > AP65(15Mn) alloy > AP65(30Mn) alloy. This shows good agreement with those relationships of potentiodynamic polarization, galvanostatic polarization, hydrogen evolution and mass loss. The second small capacitive loop is generally attributed to the diffusion of ions through the oxide or hydroxide layer [23].

Equivalent circuit used in the analysis is shown in Fig. 6(b). R_s is the electrolyte resistance; CPE_{dl} is the double layer capacitance between the electrode and the electrolyte phase; R_t is the charge transfer resistance; CPE_f is the dielectric capacitance of the membrane and R_f is the membrane resistance. Contribution of CPE_{dl} falls to naught at high frequencies. Most of the current is

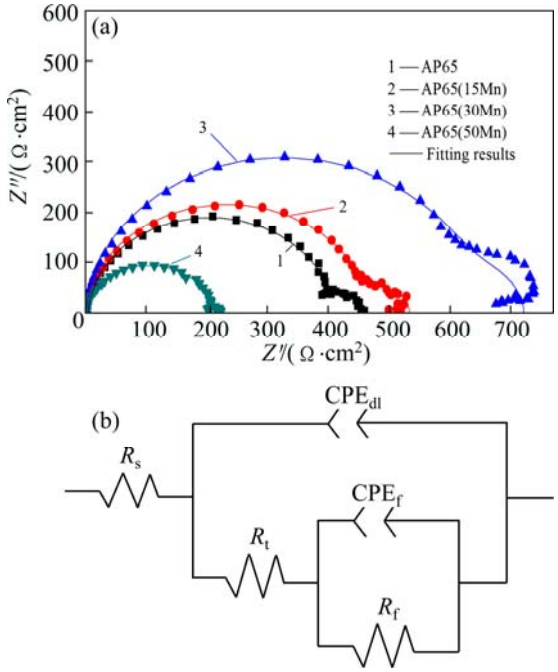

Fig. 6 Nyquist plots (a) and equivalent circuit (b) of AP65 alloys at open circuit

charge current, and the only impedance is the ohmic resistance. As the frequency drops, the finite impedance of CPE_{dl} manifests itself. At very low frequencies, the capacitance of CPE_{dl} offers a high impedance. Hence the current flow passes mostly through R_s, R_t and R_f. Thus the imaginary impedance component falls off again. The branch involving CPE_f and R_f is used to account for the transfer of charge across the membrane boundaries.

The equivalent circuit components are fitted and listed in Table 4. All of alloys rarely have distinctness in view of CPE_{dl} and CPE_f, which suggests that the capacitance plays few roles on electrochemical activity. In contrast, the odds are overt in aspect of R_t. The R_t values of AP65, AP65(15Mn), AP65(30Mn) and AP65(50Mn) alloys are 400 Ω·cm^2, 465 Ω·cm^2, 635 Ω·cm^2 and 210 Ω·cm^2, respectively. It is inferred that the extent of corrosion product attached to the surface of alloys augments in the following order: AP65(30Mn) alloy < AP65(15Mn) alloy < AP65 alloy < AP65(50Mn) alloy. AP65(50Mn) alloy sustains lager active exterior, which maybe explain its better activity.

Table 4 Electrochemical parameters of as-cast AP65 alloys obtained by fitting analysis of EIS at open circuit potential

Alloy	R_s/ (Ω·cm^2)	R_t/ (Ω·cm^2)	R_f/ (Ω·cm^2)	CPE_{dl}-T/ (Ω·cm^{-2}s^n)	CPE_{dl}-P/ ($0<n<1$)	CPE_f-T/ (Ω·cm^{-2}s^n)	CPE_f-n/ ($0<n<1$)
AP65	2	400	52	9	0.97	2000	1
AP65(15Mn)	0.8	465	68	10	0.955	2000	1
AP65(30Mn)	1.5	635	85	9	0.97	800	1
AP65(50Mn)	0.9	210	15	11	0.93	20000	1

3.3 Immersion test and mass loss

Figure 7 shows the corrosion rate as measured by the hydrogen evolution volume. It does not take oxygen contribution to cathodic reaction into account [24]. Most specimens exhibit an increase in hydrogen evolution volume with increasing immersion time. The maximum and minimum free corrosion rates are for AP65(30Mn) alloy and AP65(50Mn) alloy, respectively. AP65 alloy has better corrosion resistance than AP65(15Mn) and AP65(30Mn) alloys.

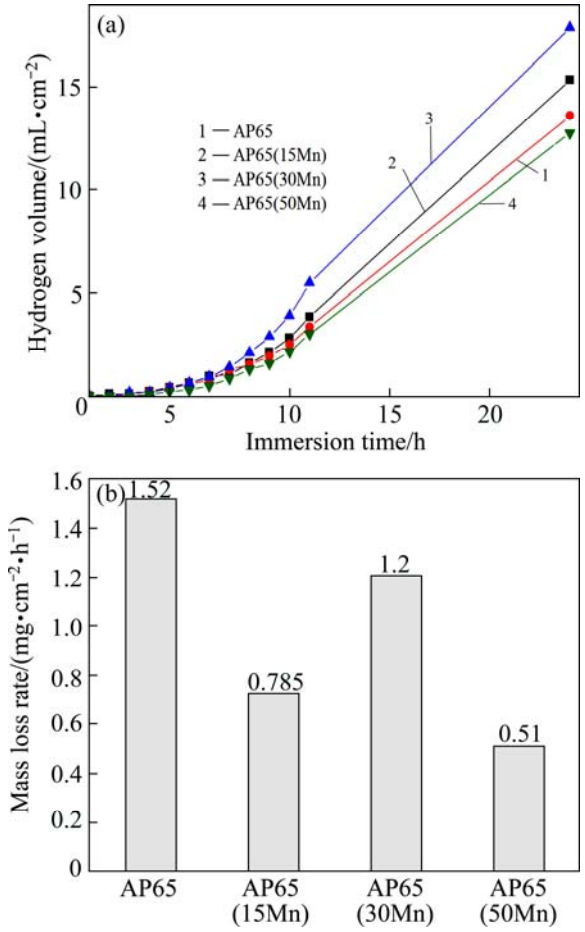

Fig. 7 Hydrogen evolution volume (a) and mass loss (b) of AP65 alloys

3.4 Corrosion morphology and corrosion mechanism

Figure 8 shows corroded surface morphologies of AP65(50Mn) alloy discharged at 180 mA/cm^2 current density for 5 s. Chloride ions can penetrate the magnesium protective film, and finally form pitting corrosion, which is their common corrosion mechanism. Small amounts of dissolved salts break down the protective film locally and result in pitting corrosion [6,24]. Pits are often formed due to selective attack along the grain boundary. Moreover, there is an tendency for micro-galvanic corrosion in all multi-phase Mg alloys since all known second phases have corrosion potentials more positive than that of magnesium matrix [7].

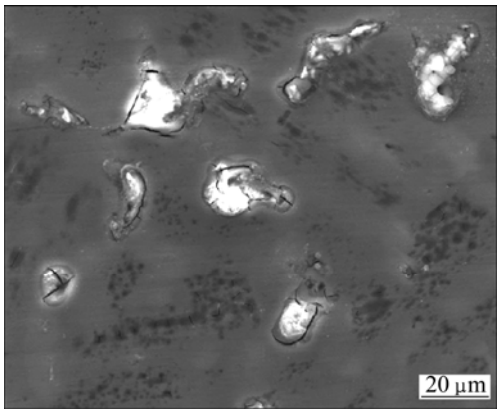

Fig. 8 SEM morphology of corroded surface of AP65(50Mn) alloy discharged at 180 mA/cm^2 for 5 s

During the corrosion process, corrosion product $Mg(OH)_2$ film can impede the corrosion to penetrate into the magnesium matrix. However, the concentration of chloride ions in seawater can accelerate the dissolution rate by transforming the formed $Mg(OH)_2$ into more soluble $MgCl_2$. Chloride ions accelerate the electrochemical reaction. Thus, the surface morphology of specimens becomes spumous and rimous as shown is Figs. 9(a) and (b). The corrosion product of AP65 alloy is loose and the corrosion product of AP65(50Mn) alloy is relatively compact. The corrosion surface of AP65(50Mn) alloy accelerates the breakdown of $Mg(OH)_2$ layer more easily and enlarges the film-free area exposure to seawater than that of AP65 alloy, which facilitates the magnesium dissolution and boosts the electrochemical activity. Compact and rimous surface is beneficial to keeping continuous corrosion reaction and provide stable potential of the AP65 anode.

Figure 10 shows the SE corroded cross-sectional morphologies of AP65 and AP65(50Mn) alloys immersed for 36 h. The β phase and Al−Mn particles act as galvanic cathode. Some regions of α matrix have corroded preferentially in the vicinity of the second phase to a considerable depth at the particle boundary by galvanic corrosion. That leads to the undermining and falling out of second phases. Then two kinds of corrosion morphologies are formed: the primary α grain is preferentially dissolved; and the second phases are undermined [7]. There are magnesium/aluminum hydroxide at the solution/film interface, magnesium/aluminum oxide at the alloy/film interface and the inner layer is Al_2O_3 on the α grain [6]. Obviously, AP65 alloy is corroded far deeper than AP65(50Mn) alloy. Their average corrosion depths are 390.87 and 194.43 μm, respectively. Corrosion product of AP65(50Mn) alloy is thicker than that of AP65 alloy. This is attributed to the microstructure of them. The microstructure of AP65 alloy has some micro-pores (see Fig. 3(a)), which

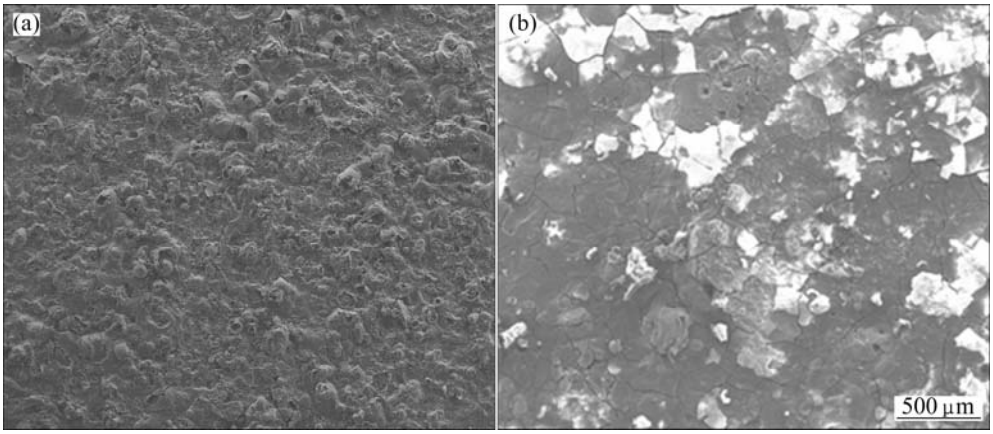

Fig. 9 SEM morphologies of corroded surface of AP65 (a) and AP65(50Mn) (b) alloys discharged at 180 mA/cm^2 for 600 s without removing corrosion products

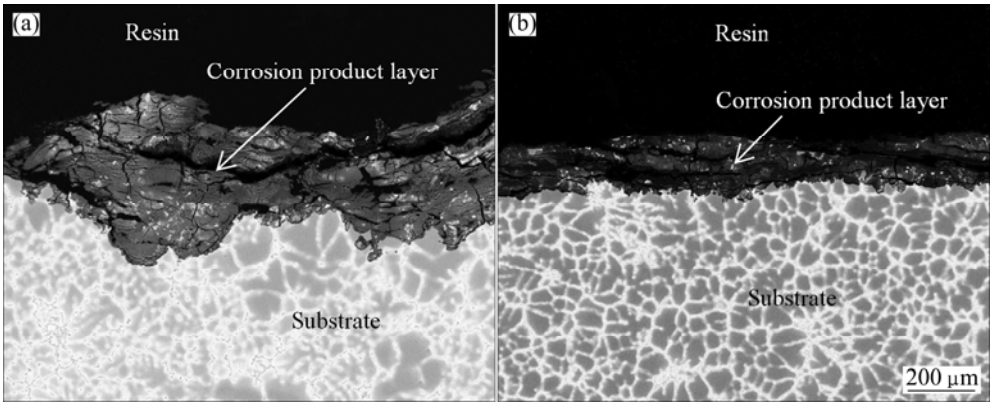

Fig. 10 SEM morphologies of corroded cross-section of AP65 (a) and AP65(50Mn) (b) alloys immersed for 36 h

increases the local corrosion. Manganese element can greatly inhibit the adverse effect of some impurity elements (such as iron, nickel). Manganese combines with the iron in the molten magnesium alloy and forms intermetallic compound, which settles to the melt bottom, thereby the iron content of the AP65 alloys is lower. Manganese encapsulates the iron particles. The galvanic activity between iron and magnesium is abated [25]. In addition, manganese form $Al_{11}Mn_4$ phase which refines grain size (see Figs. 3(a) and (b)) favors the self-peeling of corrosion products and enlarges the electrochemical reaction area as well as enhances the electrochemical activity. The addition of manganese in the forming of AP65(50Mn) master alloy can improve the protective properties of the surface film. As a consequence, AP65(50Mn) alloy is less susceptible to corrosion than AP65 alloy.

4 Conclusions

1) The mean potentials of AP65, AP65(15Mn), AP65(30Mn) and AP65(15Mn) alloys are −1.59 V, −1.54 V, −1.41 V and −1.66 V(vs SCE), respectively. Their corrosion current densities are 10, 17, 24.6 and 7 μA/cm^2, respectively.

2) AP65(50Mn) alloy has the lowest self-corrosion rate (0.51 mg/(h·cm^2)) and thinnest corrosion product (194.43 μm). AP65, AP65(15Mn), AP65(30Mn) and AP65(50Mn) alloys have similar EIS shape with a little difference in the R_t. This means they have common corrosion mechanism. Potentiodynamic polarization studies demonstrate that the corrosion of AP65 alloys in NaCl electrolyte is anodically controlled.

3) AP65(50Mn) alloy has most splendid electrochemical activity and property. This is perhaps attributed to its uniform microstructure, the presence of $Al_{11}Mn_4$ phase and compact and rimous corroded morphology. $Al_{11}Mn_4$ phase facilitates the self-peeling of corrosion products and enlarges the electrochemical reaction area.

References

[1] FENG Yan, WANG Ri-chu, YU Kun, PENG Chao-qun, LI Wen-xian. Influence of Ga and Hg on microstructure and electrochemical corrosion behavior of Mg alloy anode materials [J]. Transactions of

Nonferrous Metals Society of China, 2007, 17(6): 1363−1366.
[2] LIU Xian-bin, SHAN Da-yong, SONG Ying-wei, HAN En-hou. Effects of heat treatment on corrosion behaviors of Mg−3Zn magnesium alloy [J]. Transactions of Nonferrous Metals Society of China, 2010, 20(7): 1345−1350.
[3] LINDEN D, REDDY T B. Handbook of batteries [M]. New York: McGraw-Hill, 2002: 489−515.
[4] YANG Yue, WU Hua. Effect of current density on corrosion resistance of micro-arc oxide coatings on magnesium alloy [J]. Transactions of Nonferrous Metals Society of China, 2010, 20: 688−692.
[5] ZHAO J, YU K, HU Y, LI S, TAN X, CHEN F,YU Z. Discharge behavior of Mg−4wt%Ga−2wt%Hg alloy as anode for seawater activated battery [J]. Electrochimica Acta, 2011, 56(24): 8224−8231.
[6] SONG G L, ATRENS A. Corrosion mechanisms of magnesium alloys [J]. Advanced engineering materials, 2000, 1(1): 11−33.
[7] SONG G, ATRENS A. Understanding magnesium corrosion—A framework for improved alloy performance [J]. Advanced Engineering Materials, 2004, 5(12): 837−858.
[8] GU X, ZHENG Y, CHENG Y, ZHONG S, XI T. In vitro corrosion and biocompatibility of binary magnesium alloys [J]. Biomaterials, 2009, 30(4): 484−498.
[9] PARDO A, MERINO M, COY A, VIEJO F, ARRABAL R, FELI S. Influence of microstructure and composition on the corrosion behaviour of Mg/Al alloys in chloride media [J]. Electrochimica Acta, 2008, 53(27): 7890−7902.
[10] CANDAN S, UNAL M, TURKMEN M, KOC E, TUREN Y, CANDAN E. Improvement of mechanical and corrosion properties of magnesium alloy by lead addition [J]. Materials Science and Engineering A, 2009, 501(1): 115−118.
[11] SUDHOLZ A, BIRBILIS N, BETTLES C,GIBSON M. Corrosion behaviour of Mg-alloy AZ91E with a typical alloying additions [J]. Journal of Alloys and Compounds, 2009, 471(1): 109−115.
[12] SMITH A. The isothermal growth of manganese precipitates in a binary magnesium alloy [J]. Acta Metallurgica, 1967, 15(12): 1867−1873.
[13] YE H Z, LIU X Y. In situ formation behaviors of Al_8Mn_5 particles in Mg−Al alloys [J]. Journal of Alloys and Compounds, 2006, 419(1): 54−60.
[14] JÖNSSON M, THIERRY D,LEBOZEC N. The influence of microstructure on the corrosion behaviour of AZ91D studied by scanning Kelvin probe force microscopy and scanning Kelvin probe [J]. Corrosion Science, 2006, 48(5): 1193−1208.
[15] PENG C, MA Q, DAVID H S. Effect of manganese on grain refinement of Mg−Al based alloys [J]. Scripta Materialia, 2006, 54(11): 1853−1858.
[16] WANG Nai-guang, WANG Ri-chu, PENG Chao-qun, FENG Yan. Effect of manganese on discharge and corrosion performance of magnesium alloy AP65 as anode for seawater-activated battery [J]. Corrosion, 2012, 68(5): 388−397.
[17] WANG Y, XIA M, FAN Z, ZHOU X,THOMPSON G. The effect of Al_8M_5 intermetallic particles on grain size of as-cast Mg–Al–Zn AZ91D alloy [J]. Intermetallics, 2010, 18(8): 1683−1689.
[18] BLÜCHER D B, SVENSSON J E, JOHANSSON L G, ROHWERDER M,STRATMANN M. Scanning Kelvin probe force microscopy—A useful tool for studying atmospheric corrosion of MgAl alloys in situ [J]. Journal of The Electrochemical Society, 2004, 151(12): B621−B626.
[19] UDHAYAN R,BHATT D P. On the corrosion behaviour of magnesium and its alloys using electrochemical techniques [J]. Journal of Power Sources, 1996, 63(1): 103−107.
[20] WANG Nai-guang, WANG Ri-chu, PENG Chao-qun, FENG Yan. Corrosion behavior of magnesium alloy AP65 in 3.5% sodium chloride solution [J]. Journal of Materials Engineering and Performance, 2012, 21(7): 1300−1308.
[21] MATHIEU S, RAPIN C, HAZAN J, STEINMETZ P. Corrosion behaviour of high pressure die-cast and semi-solid cast AZ91D alloys [J]. Corrosion Science, 2002, 44(12): 2737−2756.
[22] WANG Nai-guang, WANG Ri-chu, PENG Chao-qun, FENG Yan, CHEN Bin. Effect of hot rolling and subsequent annealing on electrochemical discharge behaviour of AP65 magnesium alloy as anode for seawater activated battery [J]. Corrosion Science, 2012, 64: 17−27.
[23] TURGOOSE S,COTTIS R. The impedance response of film-covered metals [M]. ASTM International: ASTM Special Technical Publication, 1993: 173−191.
[24] FROATS T K A A, HAWKE D, UNSWORTH W, HILLIS J. Metals handbook [M]. ASM International: The Materials Information Company, 1987.
[25] LUNDER O, AUNE T K, NISANCIOGLU K. Effect of Mn additions on the corrosion behavior of mould-cast magnesium ASTM AZ91 [J]. Corrosion, 1987, 43(5): 291−295.

Al−Mn 中间合金对 Mg−Al−Pb−Mn 合金组织和电化学性能的影响

陈 彬，王日初，彭超群，冯 艳，王乃光

中南大学 材料科学与工程学院，长沙 410083

摘 要：Mg−Al−Pb 合金是一种新开发的海水激活电池材料。采用熔炼浇注法制备 Mg−6Al−5Pb−0.5Mn 系列合金和 Mg−6Al−5Pb 合金。其中，Mg−6Al−5Pb−0.5Mn 系列合金是以 Al−15%Mn、Al−30%Mn 和 Al−50%Mn 中间合金为添加剂制备的。采用金相显微镜和扫描电子显微镜表征其组织，采用电化学方法、析氢法和失重法研究其性能。结果表明：以 Al−50%Mn 中间合金为添加剂制备的 Mg−6Al−5Pb−0.5Mn 合金具有最负的放电电位(−1.66 V)，最小的腐蚀电流密度(7 μm/cm^2)和自腐蚀速率(0.51 mg·h^{-1}·cm^{-2})。这可能是因为 $Al_{11}Mn_4$ 相的存在，不仅有利于腐蚀产物的脱落和增大电化学反应面积，而且也提高电化学活性。

关键词：Al−Mn；中间合金；Mg−Al−Pb−Mn；析氢；腐蚀；水激活电池

(Edited by Chao WANG)